

Article

A Novel Classification Method for Pores in Laser Powder Bed Fusion

Natan Nudelis ^{1,2,*}  and Peter Mayr ² ¹ FIT AG, Am Grohberg 1, 92331 Lupburg, Germany² Chair of Materials Engineering of Additive Manufacturing, Technical University of Munich, Boltzmannstr. 15, 85748 Garching, Germany; peter.mayr@tum.de

* Correspondence: natan.nudelis@pro-fit.de

Abstract: Nowadays, additive manufacturing (AM) using laser powder bed fusion (LPBF) is acknowledged for its ability to generate near-net-shape components for various industries such as aerospace, automotive, and health industries. However, internal defects seem to be the inevitable concomitant in the current state of laser powder bed fusion of Al alloys. Hence, knowledge of the formation, different types, and morphologies of pores and their suppression is an essential element for successful future AM applications. The purpose of this research is to qualify a new approach of defect classification using X-ray tomography. In this framework, this research examined the influence of size, shape, and location of pores on crack initiation for AlSi10Mg parts produced by LPBF. For this reason, a total number of 39,228 pores detected in a cylindrical sample were categorised. Additionally, 26 selected pores of different morphology from the X-ray scan were analysed by means of finite element analysis (FEA). Moreover, fracture mechanics determinations were carried out to examine the correlations between pore characteristics and degree of stress concentration. The result is an evaluated novel pore classification method that can be used for process adjustments, quality assurance, as well as further research.



Citation: Nudelis, N.; Mayr, P. A Novel Classification Method for Pores in Laser Powder Bed Fusion. *Metals* **2021**, *11*, 1912. <https://doi.org/10.3390/met11121912>

Academic Editor: Matteo Benedetti

Received: 24 October 2021

Accepted: 23 November 2021

Published: 26 November 2021

Publisher's Note: MDPI stays neutral with regard to jurisdictional claims in published maps and institutional affiliations.



Copyright: © 2021 by the authors. Licensee MDPI, Basel, Switzerland. This article is an open access article distributed under the terms and conditions of the Creative Commons Attribution (CC BY) license (<https://creativecommons.org/licenses/by/4.0/>).

Keywords: laser powder bed fusion; AlSi10Mg; computed tomography; finite element analysis; novel pore classification

1. Introduction

Solely the amount of porosity does not represent the component quality accurately enough. Several parts with the same amount of porosity can show totally different mechanical properties or fatigue lives [1]. For example, smaller defect sizes often correlate with longer fatigue lives [2]. This is due to the fact that different pore sizes, shapes, and locations cause different stress intensity factors (SIF) and stimulate the crack initiation and propagation differently. Therefore, the correlations among pore shape, size, and location on the crack initiation need to be investigated. In addition, knowledge about the so-called killer pores, which ultimately lead to failure, can be useful to predict the location of the highest vulnerability. Additionally, the formation of pores is heavily dependent on the applied process parameters (e.g., laser power, hatch distance, layer thickness, scanning speed, scanning strategies, etc.) and the process conditions (e.g., powder, inert gas, etc.).

The research hypothesis of this work is that analysing and classification of porosity is essential in fostering an increased understanding of the laser powder bed fusion process and enables quality improvements by process adjustments.

The objectives of this research can be summarised as follows:

- To develop a pore classification method using computed tomography (CT) to classify the pores according to their morphology and location;
- To identify killer pores as the origin of component failure;
- To clarify the influence of pore shape, size, and location on crack initiation.

Pore Types in AlSi10Mg Components Using Laser Powder Bed Fusion

Past research has focused extensively on exploring and explaining the existing types of pores in the LPBF process, in which three types of pores are most frequently mentioned. These pore types can be categorised into spherical and irregular-shaped classes. Hydrogen-induced pores and keyhole pores can be distinguished by their spherical shape. In contrast to these, the so-called lack-of-fusion pores show highly irregular shapes. Other than the mentioned influence on the mechanical properties, the pore type can also provide detailed information about the process condition. Regarding hydrogen-induced porosity, many investigations were made. Weingarten et al. [3] showed that the gas content of the pores initiated by laser powder bed fusion (AlSi10Mg) can rise up to 96 vol%. Furthermore, Weingarten et al. [3] described two hydrogen sources appearing in the LPBF process. More than half of the measured hydrogen was bound in the moisture on the surface of the powder particles. A significant amount of hydrogen was found trapped in the powder material. It seems obvious that the high amount of hydrogen easily exceeds the solubility limit in liquid aluminium, which then forms a high number of hydrogen-induced pores during solidification. Aboulkhair et al. [4] described gas porosity as spherically shaped and small in size (less than 100 μm in diameter), preferably formed at slow scanning speeds from hydrogen trapped within the melt pool. The formation of hydrogen-induced pores is illustrated in Figure 1. The nucleation and growth of hydrogen-induced pores depend on the local hydrogen content and maximum solubility in the melt and reduced solubility in solidified aluminium. Due to the fact that hydrogen solubility in solid pure aluminium is about a factor 10 lower than in the liquid melt pool, hydrogen is enriched at the solidification front, if the hydrogen content is higher than solubility in the solid phase [3].

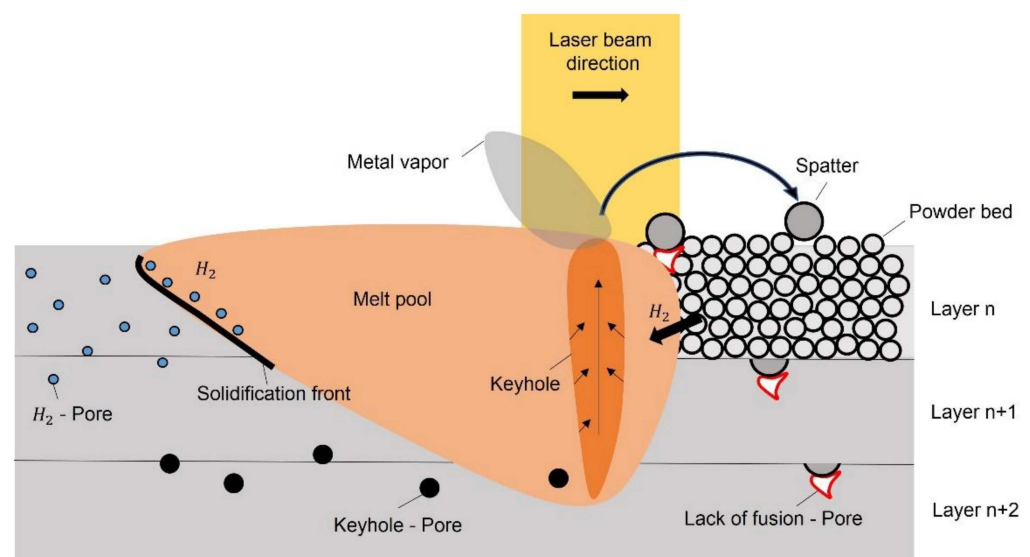


Figure 1. Formation of hydrogen-induced, keyhole, and lack-of-fusion pores during laser powder bed fusion (inspired by Weingarten et al. [3], Aboulkhair et al. [4], King et al. [5], and Haeckel et al. [6]).

Apart from hydrogen-induced pores, so-called keyhole pores exist, which are also spherical in shape but larger in diameter. Moreover, the formation mechanism and trapped gas content are different. Under certain process conditions, the mechanisms of melting can change to the so-called keyhole-mode laser beam melting, which is controlled by the evaporation of metal [5]. Keyhole pores occur when the power density of the laser beam is high enough to cause metal evaporation. The collapse of originating vapor cavities can finally leave voids in the root of the melt pool (formation illustrated in Figure 1). Hence, the trapped gas content of keyhole pores is similar to the gas used in the process chamber.

Furthermore, lack-of-fusion pores occur due to an insufficient laser energy input in the powder bed (formation illustrated in Figures 1 and 2). This results in incomplete melting and forms irregular-shaped pores, partially filled with unmolten powder particles. Haeckel et al. [6] observed, for example, weld spatter as the origin of lack-of-fusion porosity. Those particles have diameters between 200 and 500 μm and a volume many times higher than the average powder particle. Hence, those particles would need far more laser energy to be entirely melted, which is not provided by the process. Hence, this leads to an unmolten gap without fusion (i.e., lack-of-fusion pore) located directly below the weld spatter. Moreover, lack-of-fusion pores can occur due to the presence of oxide particles which release oxygen by dissociation during exposure to heat (formation illustrated in Figure 2). The volume of oxides, which cause the oxide-driven porosity, can have different origins. The processing chamber is usually filled with argon as inert or nitrogen as unreactive gas. This gas atmosphere still contains a residual amount of oxygen (0.1–0.2 vol%) which is high enough to start an oxidation process on each of the scanned layers and also at the boundaries of the melt pool [7]. The result is a network of oxide layers, partly broken up or vaporised during the melting process. Some reports have been published on oxidation during laser powder bed fusion. Louvis et al. [7] showed a wide network of oxide layers in deeply etched aluminium (6061) samples. Tang et al. [2] observed oxide particles most often at pore interfaces. In both cases, significant volumes of oxides incorporated into the parts were found. Apart from the residual oxygen in the atmosphere, the powder itself can also introduce more oxides. Oxides can also disturb the melting process and process stability and lead to a lack-of-fusion porosity (Figure 2).

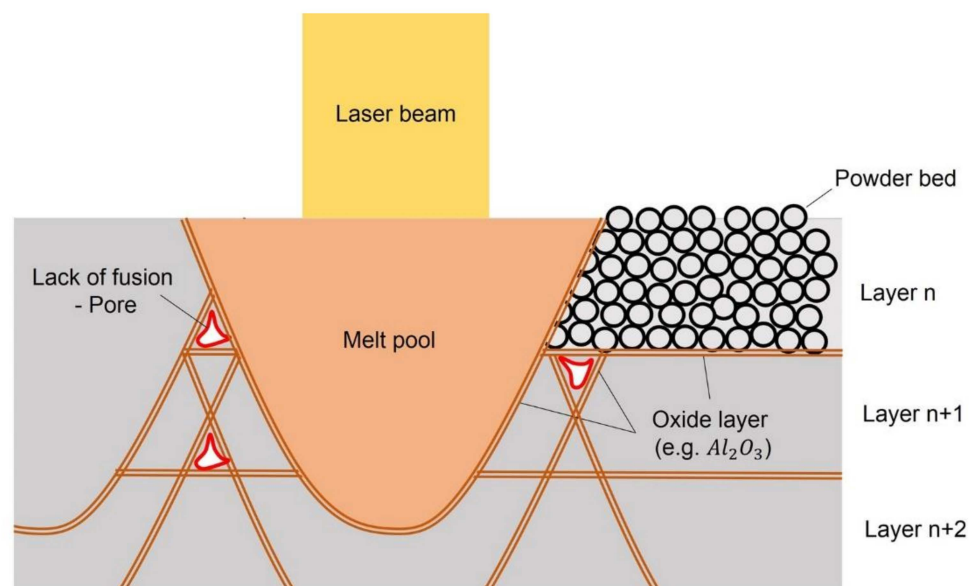


Figure 2. Formation of lack-of-fusion porosity due to the presence of oxide layers (inspired by Tang et al. [2] and Louvis et al. [7]).

The fundamentals of most types of pores are already well understood. In Addition, various destructive or non-destructive techniques are already applied for the determination of density or for pore analysis. For instance, the Archimedean method, micro sectioning, or ultrasonic methods [8] are available. Moreover, X-ray tomography has already proven its ability as a powerful and non-destructive tool to analyse defects in AM parts [1,9–12]. Due to a lack of evaluation methods, these very useful scanning data could not be used efficiently enough. Several studies tried to analyse pores by means of shape descriptors such as sphericity and aspect ratio [13], while others also used dimensional descriptors based on the bounding box or the Feret calliper method [14]. The problem so far is that either they used it only for 2D image analysis or investigated the 3D geometry in many specific shape

classes. Another approach is to use machine learning for pore classification. Snell et al. [15] classified pores using unsupervised machine learning methods, such as K-means clustering. Unsupervised learning is a very interesting approach to classify pores without prior knowledge about the used data set. Nevertheless, the classification accuracy could be further improved with supervised machine learning methods (e.g., neural networks), which need already labelled data to train a model. The suggested classification method using X-ray data can be used to provide a huge amount of labelled data for supervised learning applications. As already mentioned, keyhole- or hydrogen-induced pores are spherically shaped, whereas lack-of-fusion pores are most likely irregularly shaped. Defining a reliable pore classification in spherical and irregular-shaped groups, with as few misclassifications as possible, is a challenging task. The purpose of this paper is to provide a reliable method of defect evaluation, which uses X-ray data to classify pores. It allows an accurate examination and categorisation of pores and enables the laser powder bed fusion process to be modified as needed to avoid undesired pore types and enable good mechanical properties.

2. Methods

2.1. Details of Manufacturing Process and X-ray Scan

The analysed cylindrical specimen was fabricated at FIT AG using a laser beam melting SLM500 machine (SLM Solutions, Lübeck, Germany). The building direction was chosen vertical to the building platform. The SLM500 is equipped with an Nd:YAG laser ($\lambda = 1064$ nm) with a maximum laser output of 400 W. The working point of the laser is usually at 350 W. An overview of the process parameters for the manufactured specimen is listed in Table 1. For the X-ray scans, a simple cylindrical specimen shape was chosen (10 mm in diameter, 18 mm in height). The reason for that is the symmetrical geometry, which allows scanning the part always in the same radiated wall thickness and, hence, reduces CT-artefacts. X-ray scans were made using the Diondo d2 microfocus CT-system (Hattingen, Germany), which had a minimum voxel size of $9.659 \mu\text{m}^3$. The specimen was scanned in 1500 projections in a 360° sample rotation (1.4 s integration time per projection) using a power output of 9.5 W and a voltage of 190 kV. The reconstruction of raw CT data into a 3D model was performed with VGSTUDIO MAX 3.1.0 64 (Volume graphics, Heidelberg, Germany). To analyse porosity, the VGDefx algorithm was used. The analysed region of interest (ROI) had a volume of 785.4 mm^3 .

Table 1. Overview of SLM500 process parameters for the production of cylindrical specimens.

Parameter	Value
Laser power	350 W
Laser scanning speed	1000 mm/s
Hatch spacing	0.17 mm
Spot size diameter	0.08 mm
Layer thickness	50 μm

2.2. Classification Method Using X-ray Data

For a comprehensive understanding of the formation of pores, a reliable classification method using X-ray data was developed (Figure 3). The greatest advantage of CT scans is the possibility to collect different data from each defect inside the part, which is detectable within the range of resolution. These data provide information on the position, shape, size, volume fraction, density, and quantity of pores. This allows allocating pores into different classes. For an accurate classification of pores, information about size and shape is essential. For this reason, three shape indicators, as well as diameter as the size indicator, are needed.

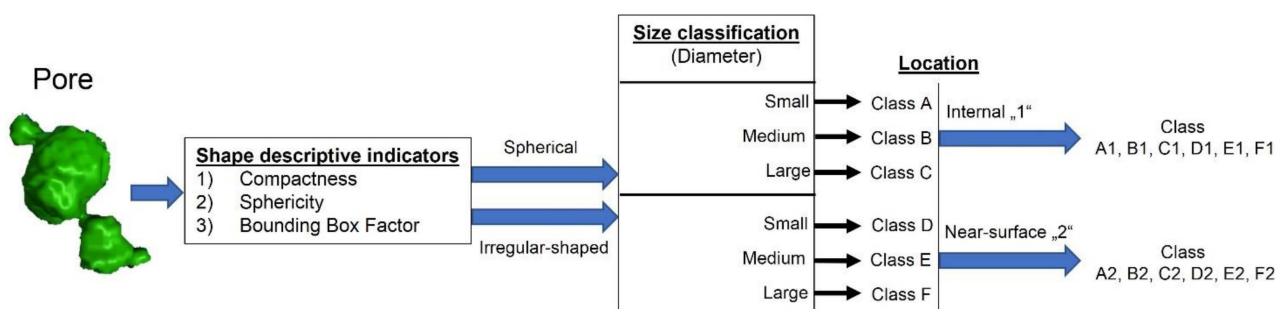


Figure 3. Pore classification procedure using X-ray data.

The first shape indicator is sphericity, which is defined as the ratio of the surface area of a sphere with the same volume as the given pore to the pore’s surface area.

$$\Psi = \frac{\pi^{\frac{1}{3}} (6 \cdot V_{pore})^{\frac{2}{3}}}{A_{pore}}, \tag{1}$$

where V_{pore} is the pore volume, and A_{pore} is the pore’s surface area.

The second shape indicator is the compactness of the pore and is expressed as the ratio of pore volume to the volume of a sphere, which is defined by the maximum diameter/radius around the pore.

$$\Omega = \frac{V_{pore}}{\frac{4}{3} \cdot \pi \cdot R_{pore}^3}, \tag{2}$$

where R_{pore} is the maximum pore radius. Additionally, bounding box dimensions can be used to classify a pore shape. On this account, three-dimensional descriptors S , M , and L must be introduced, where S is the shortest pore dimension, L is the longest pore dimension and M describes the medium-sized pore dimension. The ratios M/L and S/M are suitable to quantify the shape, as shown in Figure 4.

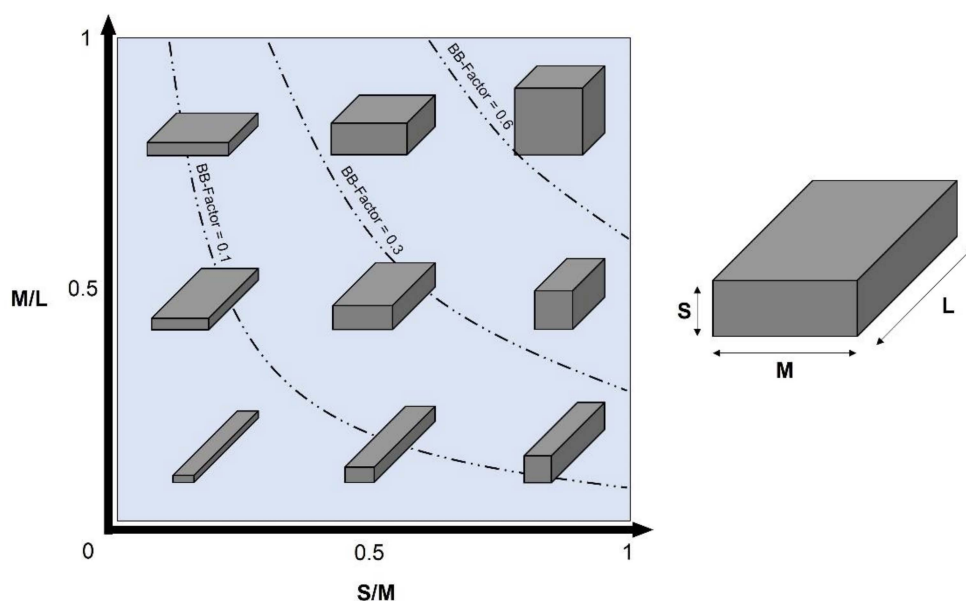


Figure 4. Definition of bounding-box factor (BB-factor).

These ratios describe the dimensional shape quite well. Nevertheless, for the used classification method, only two shape classes (spherical/irregular-shaped) are needed. Therefore, the bounding box factor (*BB factor*) is introduced as follows:

$$BB\ factor = \frac{S}{L} \quad (3)$$

The *BB factor* allows the pores to be grouped into spherical or non-spherical shapes. An irregular-shaped geometry can fit in all bounding box aspect ratios, but a spherical pore can only fit in an almost perfect bounding box aspect ratio of 1:1:1. Due to this fact, the *BB factor* proved to be an appropriate indicator for this classification. Exemplarily, three *BB factors* are plotted in Figure 4. All three shape indicators (sphericity, compactness, and *BB factor*) were used to sort the pores into spherical or non-spherical. Classification criteria are shown in Table 2. The pores are divided into six classes (A-F), where classes A-C describe spherical shaped pores and D-F describe irregular-shaped pores. Combined with the information about the pore size (diameter), the classification of pore types such as hydrogen-induced pores, keyhole pores, and lack-of-fusion pores is possible. Pore size is defined by the maximum diameter around the pore.

Table 2. Pore classification criteria using X-ray data.

Pore Class		Diameter	Compactness	Sphericity	BB-Factor	Location
Spherical	A	$D_{pore} \leq 100\ \mu\text{m}$	$\Omega \geq 0.4$	$\Psi \geq 0.6$	$BBF \geq 0.6$	Internal pore "1" ($a/h < 0.8$) Near-surface pore "2" ($a/h > 0.8$)
	B	$100\ \mu\text{m} < D_{pore} \leq 200\ \mu\text{m}$				
	C	$D_{pore} > 200\ \mu\text{m}$				
Irregular-shaped	D	$D_{pore} \leq 100\ \mu\text{m}$	$\Omega < 0.4$	$\Psi < 0.6$	$BBF = [0, 1]$	
	E	$100\ \mu\text{m} < D_{pore} \leq 200\ \mu\text{m}$				
	F	$D_{pore} > 200\ \mu\text{m}$				

a is the radius of a sphere around the pore, and h is the distance between the part surface and the pore centre. Example: spherical, small, and internal pore "A1".

All three shape indicators— Ψ , Ω , and *BB factor*—describe the shape of pores quite well but differently. Therefore, all three indicators are necessary to define the shape as accurately as possible. The reason is exemplified in Figures 5 and 6, which show 39,228 classified pores (according to the criteria in Table 2), based on their sphericity and compactness. For better understanding, the pore classification results are separated into four areas of 1–4. The criteria for a spherical pore are compactness > 0.4 , sphericity > 0.6 , and *BB-factor* > 0.6 . Hence, spherical pores only appear in area 4. The irregular-shaped pores can appear in each area, which explains the necessity to use many shape indicators combined. Without the compactness criteria, all pores in area 2 would be wrongly classified as spherical. Without the sphericity criteria, all pores in area 3 would be wrongly classified as spherical as well. Additionally, misclassifications can be reduced to a minimum with the help of the *BB factor*. Even if the criteria for a spherical pore regarding compactness and sphericity are given, the *BB factor* must be > 0.6 as well. Hence, without the *BB factor*, all irregular-shaped pores in area 4 would be wrongly classified as spherical. Generally speaking, to reduce misclassifications, all three shape indicators have to clearly categorise the same shape class.

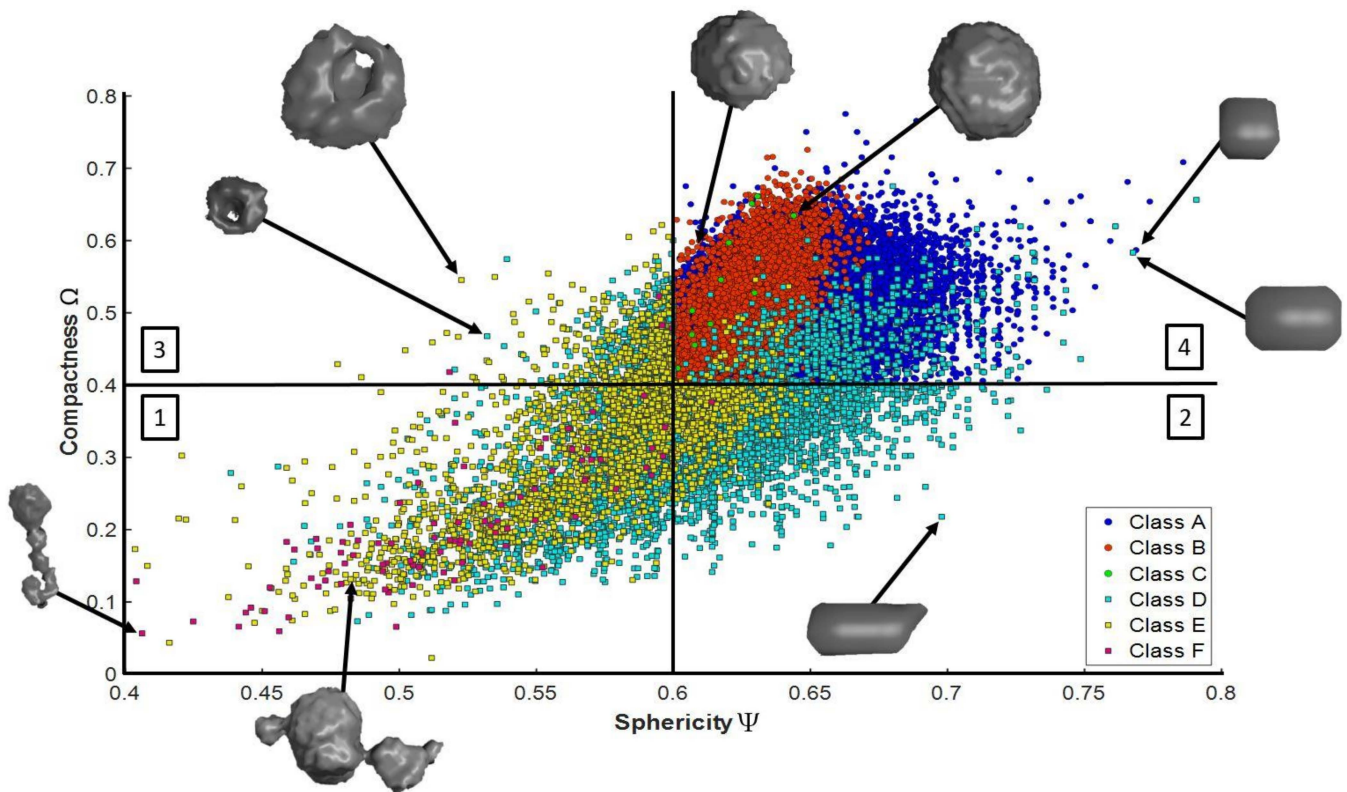


Figure 5. Pore classification of a scanned cylindrical specimen fabricated by laser powder bed fusion (details in Section 2.1). The corresponding classification areas 1, 2, 3, and 4 are according to the sphericity and compactness criteria of Table 2.

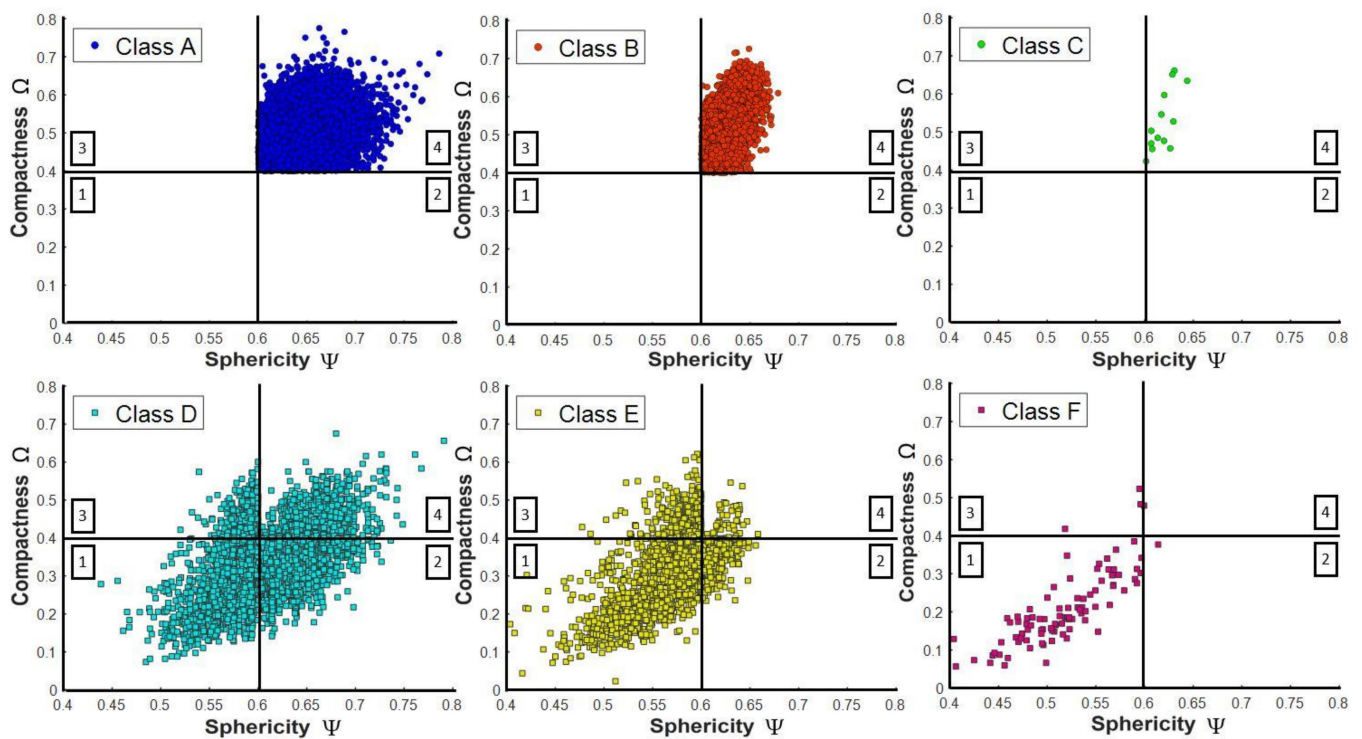


Figure 6. Pore classification of a scanned cylindrical specimen fabricated by laser powder bed fusion (details in Section 2.1). Each pore class is shown separately. The corresponding classification areas 1, 2, 3, and 4 are according to the sphericity and compactness criteria of Table 2.

2.3. Crack Initiation at Stress Concentration Sites

Du Plessis et al. [1] hypothesised that the largest pore is the origin of failure. They could also show a correlation between the failure location and the largest stress concentration. In reality, the crack formation depends on the size of the pore, but several studies have shown that surface or near-surface defects are far more critical regarding crack propagation than internal defects, even in the presence of larger internal defects [9,16,17].

Yadollahi et al. [18] showed that as-built specimens are far more critical regarding fatigue failure than specimens tested at low-stress ground (LSG) surface finish. In investigations using X-ray scans, only closed voids can be localised as pores. This is due to the fact that the software (Volume Graphics) cannot differentiate between the part surface and a surface defect. Only internal pores or near-surface pores can be recognised as pores. Consequently, the detrimental effect of roughness cannot be considered. Nevertheless, according to Murakami [19], a significant interaction between the surface and near-surface defects exists, which stimulates the crack initiation. Therefore, near-surface pores and internal pores are also distinguished. It is important to emphasise that the crack coalescence is neglected within the scope of this investigation. An empirical rule by Murakami [19] can be used to classify the pores as near-surface or internal defects.

$$\frac{a}{h} > 0.8, \quad (4)$$

where a is the radius of a sphere around the pore, and h is the distance between the part surface and the pore centre. The pore is considered as a near-surface pore when Equation (4) is confirmed. Notably, additively manufactured (AM) parts often target a lightweight design. This means the surface-to-volume ratio is usually quite high in comparison with massive components, which are rarely manufactured by laser powder bed fusion or similar. Such near-surface pores are well known to be far more detrimental than internal defects and may occur more often in AM applications than in other fields.

In terms of localising the killer pores, i.e., pores that ultimately lead to failure, stress concentration plays a prominent role. The stress at the edge of a pore has a much higher stress concentration and thus can be much higher than the externally applied stress. This observation is called ‘stress concentration’, which allows fatigue cracks most likely to grow. Murakami [20] described the defect projection area (\sqrt{area}) as the most convenient size parameter for defects because of its good correlation with the maximum stress intensity factor K_{max} at the crack front. Accordingly, the maximum stress intensity factor for a near-surface pore and an internal pore is expressed as [19]

$$K_{max} = 0.65 \cdot \sigma \sqrt{\pi \sqrt{A_{ppa}}} \text{ for a near-surface pore,} \quad (5)$$

$$K_{max} = 0.5 \cdot \sigma \sqrt{\pi \sqrt{A_{ppa}}} \text{ for an internal pore,} \quad (6)$$

where σ is the externally applied tensile load in relation to the perpendicular plane of the projected pore area A_{ppa} . In this work, the largest projected area detected at the YZ, XZ, or XY plane was used as A_{ppa} . It is worth noting that the XY planes are equal to the fabricated layers in the building direction. Interestingly, the largest projected pore areas were most frequently observed perpendicular to the manufacturing direction (XY plane).

The maximum stress intensity factor K_{max} is commonly used to approximate the stress intensity for three-dimensional cracks of indefinite shapes [19]. It does not seem inappropriate to use this definition of K_{max} also for defects such as pores. Therefore, K_{max} will be used as an indicator of the criticality of pores to initiate the final fracture. Notably, K_{max} is using an effective area which is estimated by considering a smooth contour circumscribing the original pore shape. This estimation method is illustrated in Figure 7. On this account, K_{max} might not be the perfect indicator to represent the influence of various

pore shapes. Hence, the influence of pore shapes on the crack initiation was assessed by means of FEA, which is described in Section 2.4 in more detail.

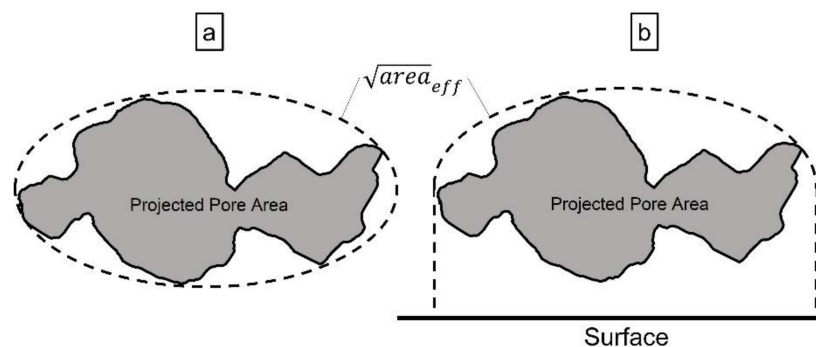


Figure 7. Definition of effective area ($\sqrt{area_{eff}}$) which is estimated by considering a smooth contour circumscribing the original pore shape in case of (a) an internal pore and (b) a near-surface pore.

As already described, the influence of size and location of pores on crack initiation is already well known. Nevertheless, the knowledge about the effect of various pore shapes on crack initiation is still quite limited.

2.4. Finite Element Analysis

Internal pores can act as highly localised stress concentrators which can cause a critical crack initiation. By examining the effect of various pore shapes on the resulting local stress intensity, this study aims to provide answers to the importance of pore shapes in relation to the effect of pore size and location.

Siddique et al. [16] already made an attempt to determine the effect of pore size and pore location on damage mechanisms. By means of FEA, they could show that the critical pore does not necessarily have to be the largest one. The distance to the surface plays an important role in the formation of stress concentrations, which possibly enhance crack growth. FE simulation seems to be an appropriate method to analyse pores relating to stress concentrations and to identify potential crack initiation sites [1,16]. On this account, FEA was used to investigate the influence of various pore shapes on the stress concentration under quasi-static tensile load.

In summary, 26 pores of various shapes were extracted from the CT scan. In order to reduce the effect of pore size, the volume of the pores was equalised to 100 mm^3 . The pores were placed into defect boxes, which are always 50% larger in size than the bounding box of the pore. Figure 8 illustrates the defect box. The tensile load was exercised perpendicular to the plane of the largest projected area. Each analysed pore was loaded vertically and horizontally related to the plane of the largest projected area. Especially in the case of highly irregular-shaped pores, the resulting stress concentration is heavily dependent on the load direction. All simulations were performed with the software Z88Aurora[®] V5 (Bayreuth, Germany) using a non-linear calculation. The STL files of the pores were transformed into a tetrahedron (quadratic) mesh using the NETGEN mesher. In non-linear analyses, different material laws can be chosen to consider elastic–plastic material behaviour. By considering plastic material behaviour (von Mises), additional material data must be specified. The material parameters for AlSi10Mg such as Young’s modulus (66.11 GPa), Poisson’s ratio (0.3897), as well as the flow curve, were taken from Sert et al. [21]. It is worth noting that the used mechanical properties were tested at samples fabricated at 90° building orientation using an SLM 280HL machine (LPBF technology). The AlSi10Mg samples were heat-treated for 4 h at 170°C . For the simulation, the part density was 2.68 g/cm^3 . The non-linear calculation was performed using the PARADISO solver with von Mises yield criterion and the Newton–Raphson solution procedure.

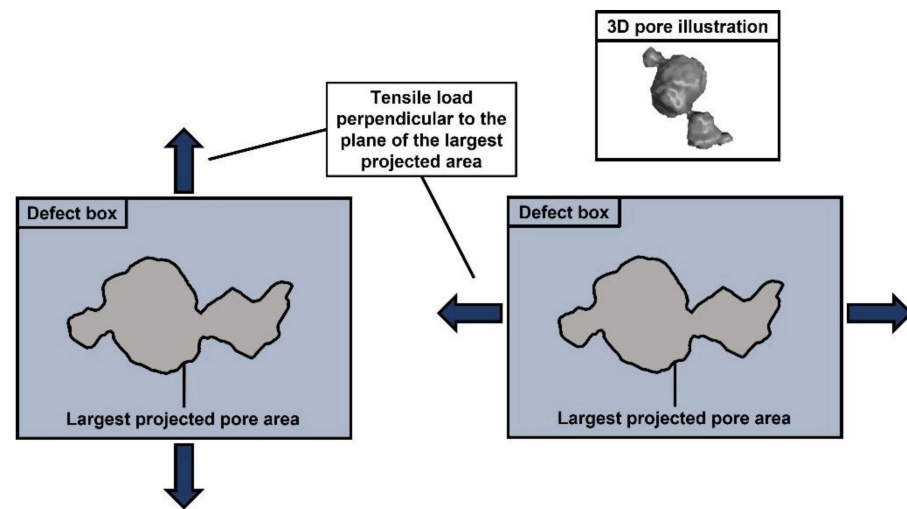


Figure 8. Illustration of a defect box and the performed tensile load perpendicular to the plane of the largest projected area.

3. Results and Discussion

3.1. Influence of Pore Shape on Stress Concentration

As already mentioned in Section 2.2, three shape indicators (Ψ , Ω , and *BB factor*) are necessary to classify pores in irregular-shaped or spherical, accurately. The effect of shape on emerging stress concentrations was analysed by means of FEA. An Overview of all 26 extracted and analysed pores is shown in Figure 9. The larger the pores are, the more voxels are available to describe the shape. Therefore, the largest pores in various shapes were chosen to analyse the interaction between shape and the emerging stress concentration. Details regarding pore extraction and preparation are summarised in Section 2.4. The results show the pore shape under various sphericities and compactness, as well as the determined maximum stress concentration. Within the scope of this work, two different load directions were separately analysed. The external tensile load was 10 N/mm^2 . Each pore was exercised vertically and horizontally related to the plane of the largest projected area (illustrated in Figure 8). The results show the exact value of sphericity and compactness cannot be used as a predictor for high-stress concentrations. For example, three pores with the same compactness (0.4–0.5) and sphericity (0.5–0.55) level show a completely different result on the emerging maximum stress concentration. Most likely, some special shapes and the load direction are responsible for the differences. Nevertheless, it seems that shape irregularity plays the most important role in emerging stress concentrations. The five highest stress concentrations (highlighted in red) were observed at sphericities below 0.55 and compactness below 0.5. The more spherical the pores become, the fewer are the number of high-stress peaks.

To build an understanding of the crack origins, the FEA of the most critical pore shapes relating to stress concentrations are illustrated in Figure 10. The highest stress concentrations seem to appear at large cross-sectional transitions. The reason for that could be the uneven elongation at different cross sections during load. As Du Plessis et al. [1] investigated, the higher the simulated stress is, the lower is the elongation before failure. The FEA analysis in this study also showed a much higher elongation at the large cross sections than at the smaller ones. These different degrees of deformation are a direct cause of the stress concentrations at areas of higher stiffness. It is important to mention that all pores with that kind of cross-sectional transition can cause a high-stress concentration.

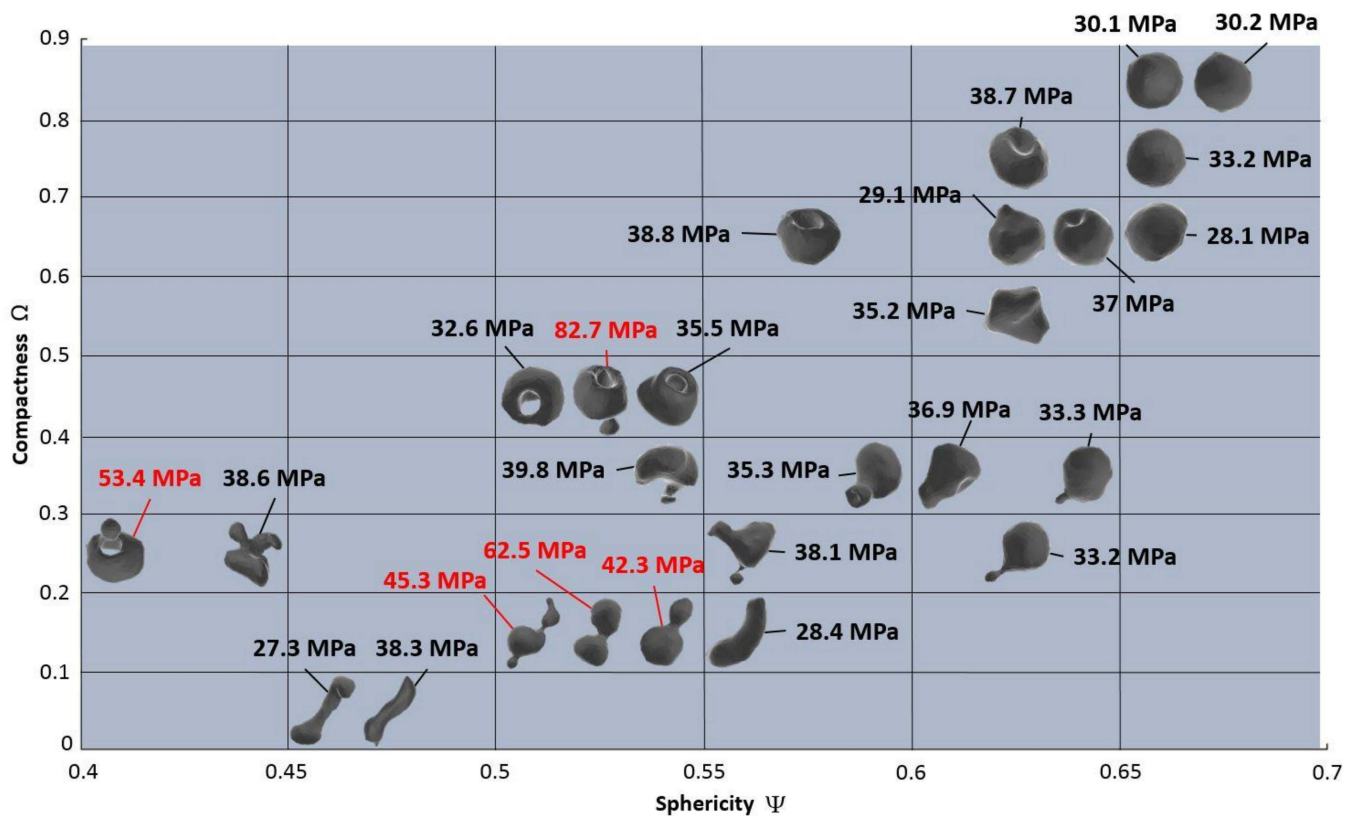


Figure 9. Overview of all 26 extracted and analysed pores from the X-ray scan in relation to their sphericity, compactness, and stress concentration.

The stress concentration is also heavily dependent on the pore geometry and the load direction [1]. In particular, irregular-shaped pores show under various load directions a totally different result in stress concentrations. In Figure 11, the FEA result of three pores (irregular and spherically shaped) under vertically or horizontally load (perpendicular to the plane of the largest projected area) are exemplified. The load direction is highlighted in yellow. Only nearly spherical pores are expected to be independent regarding the load direction. Furthermore, spherical pores do not have any cross-sectional transitions which can cause such high-stress concentrations. Therefore, it seems to be obvious that spherical pores are not the origin of high-stress concentrations and are most likely not responsible for the first critical failure. Due to this fact, the pore classification in irregular-shaped and spherical defects seems to be valid. In terms of critical failure, the knowledge about the exact geometry in irregular-shaped pores is mostly irrelevant, unless the load direction is also known. Under defined load directions, the highest stress concentrations seem to appear at pores with large cross-sectional transitions. However, the suggested classification (Section 2.2) using three shape indicators (Ψ , Ω , and *BB factor*) proves to be accurate enough to separate the critical shapes from the less critical ones.

In order to assess the FEA results, a closer look at the mesh size has to be made. To this end, several FE analyses with different mesh sizes were performed. Figure 12 shows the resulting discretised shapes, as well as the maximum stress concentration, the calculating time, and the element size of the mesh. Notably, the pore and element sizes were artificially changed. To reduce the effect of pore size, the volume of all pores was equalised to 100 mm³. No critical change in stress concentrations or singularities amongst the coarse and fine meshes were observed. Singularities are areas in the FE mesh, where the stress keeps increasing with further mesh refinement. Even with a tolerance of ± 10 MPa, all tendencies and high-stress locations are still recognisable. Typically, the smaller the mesh size is, the more accurate the result becomes. In order to compare different pore shapes, the use of a

finer mesh will probably cause fewer errors. On the other hand, the calculating time is also increasing with finer meshes. Therefore, an element size of 0.5 mm (mesh no. 5) seems to be the best choice in the context of accuracy and manageable calculating time.

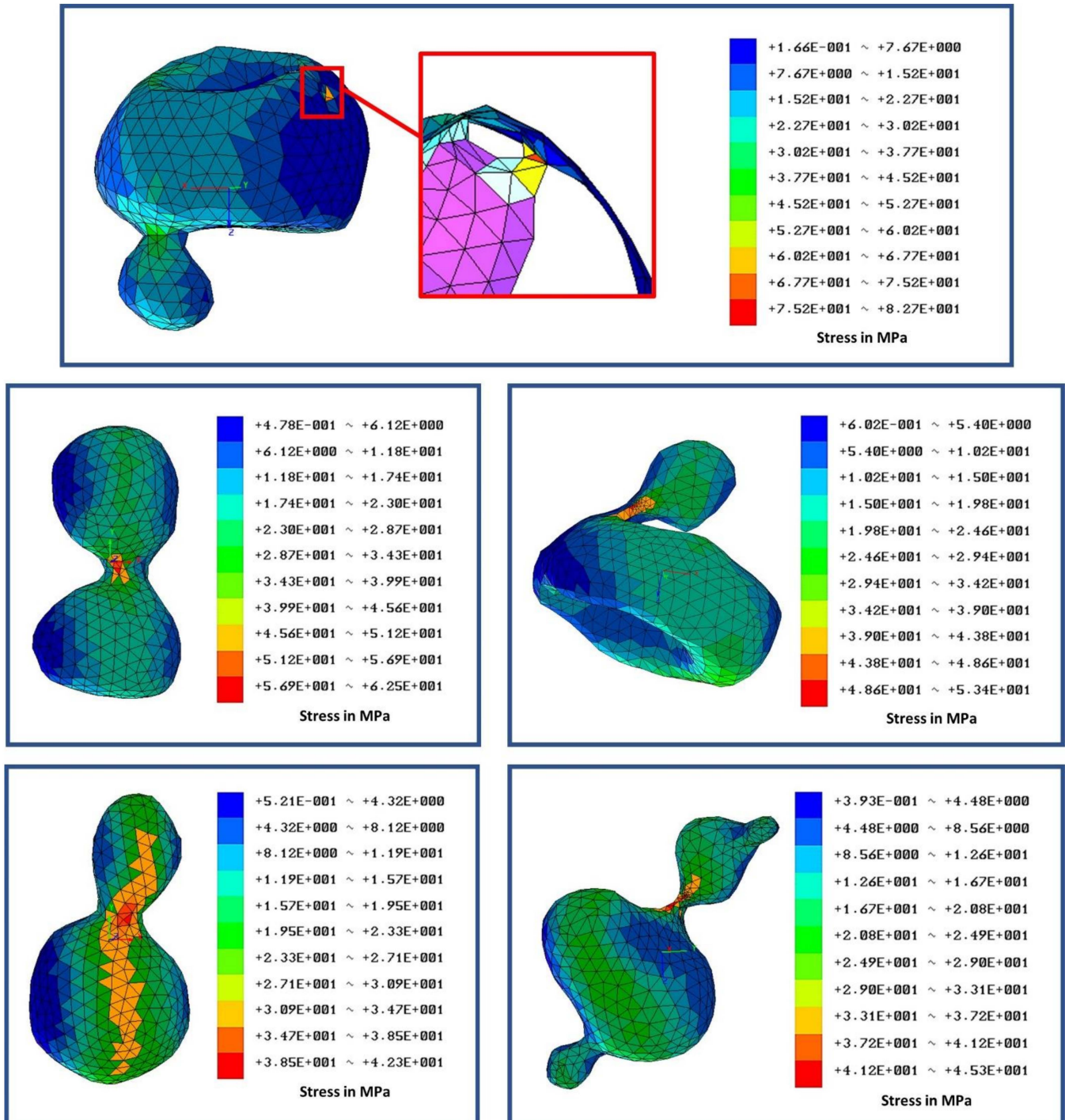


Figure 10. FE analysis of the most critical pore shapes relating to stress concentrations. Each pore was loaded vertically or horizontally related to the plane of the largest projected area. The FEA results with the highest stress concentrations are illustrated.

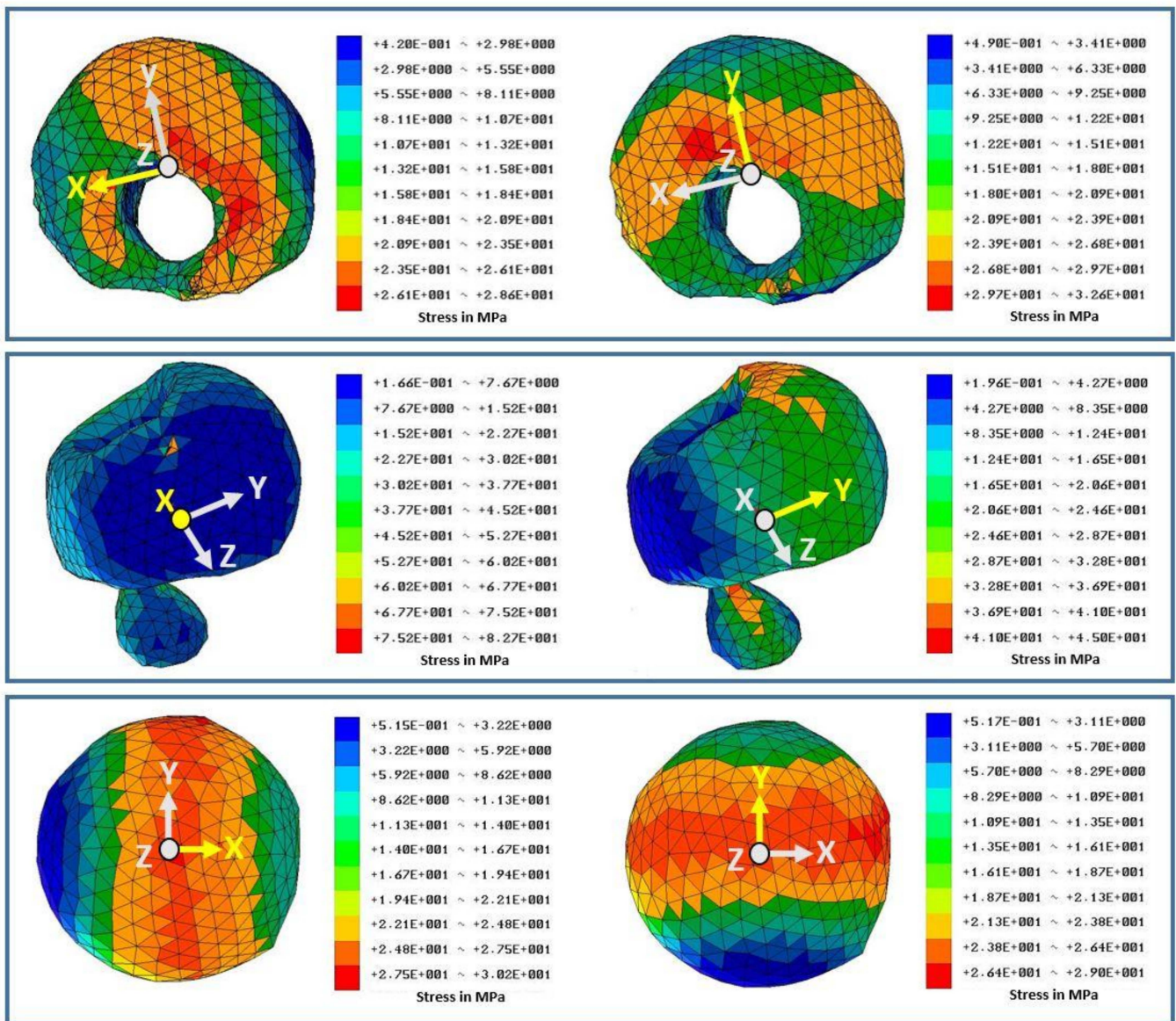


Figure 11. FE analysis of the stress level according to pore shapes under vertically or horizontally load (perpendicular to the plane of the largest projected area). The load direction is highlighted in yellow.

	1	2	3	4	5	6
Max. stress	54.9 MPa	54.1 MPa	55.1 MPa	59.9 MPa	62.5 MPa	54.6 MPa
Calculating time	51 s	1 min	1 min 44 s	3 min 5 s	14 min 35 s	36 min 36 s
Element size	1 mm	0.875 mm	0.750 mm	0.625 mm	0.5 mm	0.375 mm

Figure 12. Mesh sensitivity analysis.

3.2. Influence of Pore Size and Location on Stress Concentration

The pore size and location also dictate the criticality of defects. The influential effect of large pores or near-surface pores was already reported in many studies [1,9,16,17]. Therefore, the pore size and location play important roles in the presented pore classification. Moreover, the effect of pore size and location on the emerging stress concentration factor K_{max} were analysed by means of Equations (5) and (6). Figure 13 shows the calculated stress concentration factor K_{max} for each detected pore from the X-ray scan in relation to their pore diameter. A total number of 39,228 pores in the original size from the scanned specimen were analysed. The ultimate tensile strength of AlSi10Mg samples can achieve values of about 400 N/mm² [21]. Therefore, the external tensile load was assumed as 400 N/mm². The illustrated diagram clearly shows an almost linear behaviour of stress concentration and pore size. The stress concentration factor increases almost linearly with rising pore diameters. Du Plessis et al. [1] also observed a good correlation between large stress concentration and pore size. According to that study, the classification of pores in various pore sizes seems to be essential. The pore classification of small, medium, and large was chosen (highlighted in red lines). Furthermore, pore location was considered by means of Equation (4). It should be noted that according to Murakami's Equations (5) and (6), the stress concentration factors of near-surface pores are higher than that of internal ones. In our case, only small near-surface pores were observed. Nevertheless, these near-surface pores have the same stress concentration level as internal pores in medium sizes.

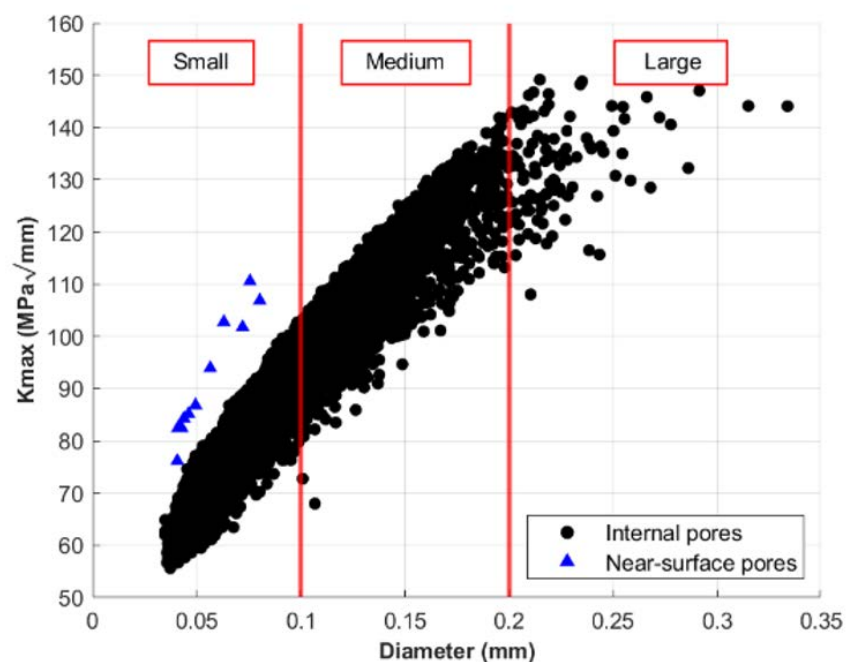


Figure 13. Calculated stress concentration factors K_{max} for each detected pore of the X-ray scan in relation to the pore diameter and location.

4. Conclusions

The formation of internal defects is heavily dependent on the applied process parameters and process conditions. Therefore, pores can be seen as an individual process fingerprint and hence act as a data source for supervised learning (SL) methods (e.g., neural networks). The presented classification method using X-ray data can be used to provide a considerable volume of labelled data for SL applications. In addition, data quality plays a decisive role. This novel classification method classified pore shape by means of three shape indicators (Ψ , Ω , and BB factor). It is important to emphasise that all three shape indicators have to be used to define the shape as accurately as possible in irregular-shaped and

spherical classes. Using the sphericity, compactness, and bounding-box factor combined will lead to a crucial reduction in pore shape misclassification.

Moreover, the effect of pore shape on emerging stress concentrations was analysed by means of FEA. The results show that the exact value of sphericity and compactness cannot be used as a predictor for high-stress concentrations. In fact, stress concentration is heavily dependent on pore shape and load direction. Especially irregular-shaped pores show under various load directions a totally different result in stress concentrations. Only spherical pores seem to be independent regarding the load direction.

In terms of critical failure, knowledge about the exact geometry in terms of irregularity is mostly irrelevant, unless load direction is also known. Under defined load directions, the highest stress concentrations seem to appear at pores with large cross-sectional transitions. It is worth mentioning that spherical pores do not have any cross-sectional transitions, which can cause such high-stress concentrations.

In reality, the external load is mostly much more complex, which is why virtually all irregular-shaped pores are a potential risk. Therefore, defining the most reliable shape classification in irregular-shaped and spherical shapes is crucial.

Large and irregular-shaped pores will dictate the occurring component failure, most often by a single dominating crack propagation. In this context, pore classes E and F, especially the ones close to the surface, are critical and should be reduced by adapted process parameters or post-processing such as hot isostatic pressing. Furthermore, pore classes E and F will represent weak spots in an AM component. Notably, the largest projected pore areas were most frequently observed perpendicular to the manufacturing direction (XY plane). Especially, loads perpendicular to the manufacturing direction (XY planes) of the part will cause high-stress concentrations and can be the source of potential crack initiations and final failures.

Finally, pore types such as hydrogen-induced pores, keyhole pores, or lack-of-fusion pores can be categorized. With that knowledge, process adjustments can be accomplished in future studies to ensure the quality of existing AM processes and improve future ones.

Author Contributions: Conceptualization, N.N. and P.M.; methodology, N.N.; software, N.N.; validation, N.N.; formal analysis, N.N.; investigation, N.N.; resources, N.N.; data curation, N.N.; writing—original draft preparation, N.N.; writing—review and editing, N.N. and P.M.; visualization, N.N.; supervision, P.M.; project administration, N.N.; funding acquisition, no additional/external funding. All authors have read and agreed to the published version of the manuscript.

Funding: This research received no external funding.

Data Availability Statement: The data presented in this study are available on request from the corresponding author.

Acknowledgments: The authors would like to thank the FIT Additive Manufacturing Group, especially Carl Fruth, for the opportunity to carry out this research in his company.

Conflicts of Interest: The authors declare no conflict of interest.

References

1. Du Plessis, A.; Yadroitsava, I.; le Roux, S.; Yadroitsev, I.; Fieres, J.; Reinhart, C.; Rossouw, P. Prediction of mechanical performance of Ti6Al4V cast alloy based on microCT-based load simulation. *J. Alloy. Compd.* **2017**, *724*, 267–274. [[CrossRef](#)]
2. Tang, M.; Pistorius, P.C. Oxides, porosity and fatigue performance of AlSi10Mg parts produced by selective laser melting. *Int. J. Fatigue* **2017**, *94*, 192–201. [[CrossRef](#)]
3. Weingarten, C.; Buchbinder, D.; Pirch, N.; Meiners, W.; Wissenbach, K.; Poprawe, R. Formation and reduction of hydrogen porosity during selective laser melting of AlSi10Mg. *J. Mater. Process. Technol.* **2015**, *221*, 112–120. [[CrossRef](#)]
4. Aboulkhair, N.T.; Everitt, N.; Ashcroft, I.; Tuck, C. Reducing porosity in AlSi10Mg parts processed by selective laser melting. *Addit. Manuf.* **2014**, *1–4*, 77–86. [[CrossRef](#)]
5. King, W.E.; Barth, H.D.; Castillo, V.M.; Gallegos, G.F.; Gibbs, J.; Hahn, D.E.; Kamath, C.; Rubenchik, A.M. Observation of keyhole-mode laser melting in laser powder-bed fusion additive manufacturing. *J. Mater. Process. Technol.* **2014**, *214*, 2915–2925. [[CrossRef](#)]

6. Haeckel, F.; Meixlsperger, M.; Burkert, T. Technological challenges for automotive series production in laser beam melting. In Proceedings of the 28th Annual International Solid Freeform Fabrication Symposium, Austin, TX, USA, 7–9 August 2017.
7. Louvis, E.; Fox, P.; Sutcliffe, C.J. Selective laser melting of aluminium components. *J. Mater. Process. Technol.* **2011**, *211*, 275–284. [[CrossRef](#)]
8. Livings, R.A.; Biedermann, E.J.; Wang, C.; Chung, T.; James, S.; Waller, J.M.; Volk, S.; Krishnan, A.; Collins, S. Nondestructive Evaluation of Additive Manufactured Parts Using Process Compensated Resonance Testing. *Struct. Integr. Addit. Manuf. Parts* **2020**, 165–205. [[CrossRef](#)]
9. Du Plessis, A.; Yadroitsava, I.; Yadroitsev, I. Effects of defects on mechanical properties in metal additive manufacturing: A review focusing on X-ray tomography insights. *Mater. Des.* **2020**, *187*, 108385. [[CrossRef](#)]
10. Romano, S.; Abel, A.; Gumpinger, J.; Brandão, A.; Beretta, S. Quality control of AlSi10Mg produced by SLM: Metallography versus CT scans for critical defect size assessment. *Addit. Manuf.* **2019**, *28*, 394–405. [[CrossRef](#)]
11. Cai, X.; Malcolm, A.A.; Wong, B.S.; Fan, Z. Measurement and characterization of porosity in aluminium selective laser melting parts using X-ray CT. *Virtual Phys. Prototyp.* **2015**, *10*, 195–206. [[CrossRef](#)]
12. Taute, C.; Möller, H.; du Plessis, A.; Tshibalanganda, M.; Leary, M. Characterization of additively manufacturing AlSi10Mg cubes with different porosities. *J. South. Afr. Inst. Min. Metall.* **2021**, *121*, 143–150. [[CrossRef](#)]
13. Maskery, I.; Aboulkhair, N.T.; Corfield, M.R.; Tuck, C.; Clare, A.T.; Leach, R.K.; Wildman, R.D.; Ashcroft, I.A.; Hague, R.J. Quantification and characterisation of porosity in selectively laser melted Al–Si10–Mg using X-ray computed tomography. *Mater. Charact.* **2016**, *111*, 193–204. [[CrossRef](#)]
14. Hastie, J.C.; Kartal, M.E.; Carter, L.N.; Attallah, M.M.; Mulvihill, D.M. Classifying shape of internal pores within AlSi10Mg alloy manufactured by laser powder bed fusion using 3D X-ray micro computed tomography: Influence of processing parameters and heat treatment. *Mater. Charact.* **2020**, *163*, 110225. [[CrossRef](#)]
15. Snell, R.; Tamas-Williams, S.; Chechik, L.; Lyle, A.; Hernández-Nava, E.; Boig, C.; Panoutsos, G.; Todd, I. Methods for Rapid Pore Classification in Metal Additive Manufacturing. *JOM* **2019**, *72*, 101–109. [[CrossRef](#)]
16. Siddique, S.; Imran, M.; Rauer, M.; Kaloudis, M.; Wycisk, E.; Emmelmann, C.; Walther, F. Computed tomography for characterization of fatigue performance of selective laser melted parts. *Mater. Des.* **2015**, *83*, 661–669. [[CrossRef](#)]
17. Romano, S.; Brückner-Foit, A.; Brandão, A.; Gumpinger, J.; Ghidini, T.; Beretta, S. Fatigue properties of AlSi10Mg obtained by additive manufacturing: Defect-based modelling and prediction of fatigue strength. *Eng. Fract. Mech.* **2018**, *187*, 165–189. [[CrossRef](#)]
18. Yadollahi, A.; Mahtabi, M.; Khalili, A.; Doude, H.; Newman, J. Fatigue life prediction of additively manufactured material: Effects of surface roughness, defect size, and shape. *Fatigue Fract. Eng. Mater. Struct.* **2018**, *41*, 1602–1614. [[CrossRef](#)]
19. Murakami, Y. *Metal Fatigue: Effects of Small Defects and Nonmetallic Inclusions*; Elsevier: Amsterdam, The Netherlands, 2002.
20. Murakami, Y. Material defects as the basis of fatigue design. *Int. J. Fatigue* **2012**, *41*, 2–10. [[CrossRef](#)]
21. Sert, E.; Schuch, E.; Öchsner, A.; Hitzler, L.; Werner, E.; Merkel, M. Tensile strength performance with determination of the Poisson's ratio of additively manufactured AlSi10Mg samples. *Mater. Werkst.* **2019**, *50*, 539–545. [[CrossRef](#)]